

Subtidal variability in the Taiwan Strait induced by combined forcing of winter monsoon and topography

Li LI^{1,2}, Xiaogang GUO¹, Enhui LIAO^{2,3} & Yuwu JIANG^{2*}

¹ Third Institute of Oceanography, State Oceanic Administration, Xiamen 361005, China;

² State Key Laboratory of Marine Environmental Science, Xiamen University, Xiamen 361005, China;

³ College of Earth, Ocean and Environment, University of Delaware, Newark, Delaware 19716, USA

Received December 8, 2016; revised September 4, 2017; accepted November 3, 2017; published online January 26, 2018

Abstract As an important channel connecting the East and South China Seas, circulations in the Taiwan Strait are strongly influenced by the East Asian monsoon and the topography of the strait, especially the Taiwan Bank (TWB), which is a remarkable topographic feature located at the southern entrance to the strait. Based on a series of pressure gauges deployed roughly 40 km offshore along the western Strait, subtidal sea-level variability under the combined impact of winter monsoon and topography was studied. The analyses show significant along-strait coherences of subtidal sea levels and their coherences with the large-scale monsoon wind for periods from 2 to 14 days. It is suggested that these fluctuations are mainly forced waves driven by the large-scale winds. In addition to the normal cross-shore wind setup, a sea-level setup in the along-strait direction is confirmed, which is induced by the combined forcing of the fluctuating winter monsoon and the blocking of the TWB. A southward current surge driven by a northerly wind event will cause a rising sea level over the TWB inducing a southward along-shore slope anomaly to the north of the TWB and a reversed slope anomaly to the south. The subtidal current through the channel to the west of the TWB is found to be influenced by the reversed slope anomalies generated via the along-shore setup.

Keywords Subtidal variabilities, Along-strait sea level setup, Taiwan Strait, Taiwan Bank

Citation: Li L, Guo X G, Liao E H, Jiang Y W. 2018. Subtidal variability in the Taiwan Strait induced by combined forcing of winter monsoon and topography. *Science China Earth Sciences*, 61, <https://doi.org/10.1007/s11430-016-9132-9>

1. Introduction

As a unique channel that connects the broad continental shelf to the east of China with the deep South China Sea (SCS) basin, the Taiwan Strait (TWS) is an important shipping lane between East Asia and the West (Figure 1). Physically, it provides a major pathway for water exchange between the East China Sea (ECS) and the SCS and thus affects the dynamics of the entire China Seas.

The TWS is roughly 300 km long. With a minimum width of roughly 150 km and an average of roughly 200 km, the TWS has a rather complex topography (Figure 1). In the

middle of the strait, there is the shallow Zhangyun Ridge (ZYR; also known as the Chang-Yuen Ridge) extending westward at about 24°N from the west coast of Taiwan to the center of the TWS. The ZYR partially separates the TWS into two segments: the Guanyin Depression to the north (also known as the Kuan-Yin Depression or simply the north basin) and the Xiapeng Depression to the south (also known as Penghu Basin or simply the south basin). The most remarkable topographic feature lies at roughly 23°N, namely the shallow Taiwan Bank (TWB) located at the southern entrance to the TWS. The TWB consists of a collection of submarine sand waves with crests at depths as shallow as roughly 10 m (Shao et al., 2011). The shallowest portion of the TWB is situated in the middle of the southern entrance

* Corresponding author (email: ywjiaing@xmu.edu.cn)

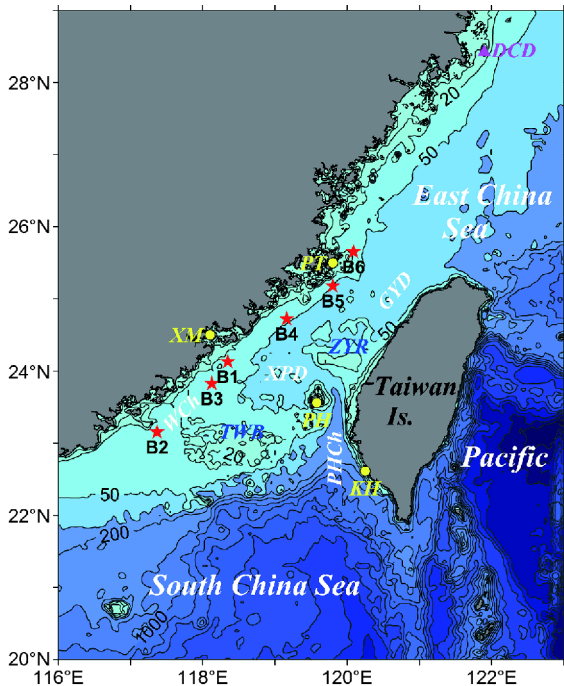


Figure 1 Topography of the Taiwan Strait showing positions of tide gauges B1 to B6 (★) and wind measurements at Dachendao (DCD, ▲). A bottom-mounted ADCP was deployed at B2 as well. TWB, Taiwan Bank; ZYR, Zhangyun Ridge; XPD, Xiapeng Depression; GYD, Guanyin Depression; PHCh, Penghu Channel; XM, Xiamen; KH, Kaohsiung; PH, Penghu; PT, Pingtan.

with channels on either side: the steep and deep (>150 m) Penghu Channel (PHCh) to the east and a gentle and shallow (~40 m) waterway to the west (referred to henceforth as WCh).

Driven by the seasonally alternating monsoon, the currents in the TWS are generally northward in summer. However, the currents are more complex in winter: the China Coastal Current flows to the south in the western strait but the currents on the other side of the strait are in the opposite direction (Hu et al., 2010; Jan et al., 2002). Meanwhile, water originating either from the SCS or the intruding Kuroshio is injected into the PHCh (Chuang, 1985, 1986; Wang et al., 2004), meandering northward and possibly even passing through the strait in a certain time period (Jan et al., 2002).

In addition to the seasonality, currents in the TWS are also subject to strong subtidal variation, which is especially energetic in winter because of the frequent passage of cold fronts over the area. Previous studies based on either tide gauges or satellite altimetry have revealed strong winter subtidal sea levels (SSLs) propagating southward along the Chinese coast and entering the TWS. Free coastal trapped waves are involved (Chen and Su, 1987; Jacobs et al., 1998; Zhao and Cao, 1987), but these contribute only a minor part of the total SSL variance measured at the west coast (Chen and Su, 1987; Li, 1989). In the TWS, the SSL fluctuation is significantly stronger along the mainland coast than it is

along the coast of Taiwan. In addition, the sea-level signals generally propagate southward along the mainland coast (Li, 1989) but travel northward on the other side (Shih et al., 1986).

Strong subtidal-current variability has been observed in several locations in the TWS (e.g., Ko et al., 2003; Lin et al., 2005; Pan et al., 2013; Wang and Chern, 1988) including the PHCh (Chuang, 1985, 1986; Hong and Wang, 2006; Wang et al., 2001, 2008). The aforementioned studies all found that subtidal-current fluctuations corresponded well with the wind variation, suggesting a predominantly wind-driven nature of the current variability. Ko et al. (2003) reported strong southward transport reversals observed in the early developing phase of the winter monsoon and demonstrated that remote wind is a major factor for the reversal. They suggested that this wind-reversal connection may be provided by free coastal trapped waves traveling along the coast from the north (Jacobs et al., 1998), although earlier studies showed that free shelf waves contribute little to the total SSL variance of the TWS.

Some (but not much) attention has been devoted in the literature to topographic effects on the dynamics of the TWS, even though its topography is rather complex. The available studies focused mainly on the ZYR in the middle reach of the TWS, which results in a cyclonic gyre to the north of the ridge in winter and leads to blocking of the northward current through the PHCh (He et al., 2015; Jan et al., 2002; Shi et al., 2015; Wang and Chen, 1989). It has also been noted that while interacting with the ZYR, the wind-driven currents can significantly change the flow pattern in the northern strait, which depends very much on the strength of the winter monsoon (Lin et al., 2005; Oey et al., 2014; Qiu et al., 2012; Wang et al., 2010, 2014). It has also been suggested that during relaxation of the northeast monsoon winds, cross-strait currents are triggered by an imbalance between pressure gradient and wind forcing, causing a cyclonic eddy to develop to the north of the ZYR as a stationary Rossby wave (Oey et al., 2014). It is somewhat surprising that even though the TWB is the most notable feature in the TWS, its topographic effect on the strait circulation has rarely been explored.

The configuration of the TWS is somehow analogous to the hydraulic problem of flows over an obstacle in a rotating channel. For a narrow strait connecting two basins, the balances for flows through the strait are between surface slope, acceleration and friction along the strait and geostrophic cross the strait (Garrett and Toulany, 1982). In addition, an obstacle, say the TWB, may cause the surface elevation to vary along the channel depending on the magnitude of the initial flow, the obstacle height, and the strength of rotation (Lane-Serff, 2004; Pratt et al., 2000). Hence, it is expected that, driven by wind and blocked by topography, water will be piled up over the TWB during cold-air outbreaks. In ad-

dition, the frequently passing cold fronts will lead to significant fluctuations of sea level over the TWB and sea-level slope along the TWS.

In this study, the aforementioned phenomena in the TWS was observed for the first time based on bottom pressure gauges deployed during winter 2007/2008. It is revealed that, in addition to the classical wind setup in the cross-shore direction, significant sea-level setup also occurs in the along-strait direction because of blocking of the wind-driven currents by the topography of the shallow TWB. Driven by the combined forcing of winter monsoon and topography, along-strait sea-level slope anomalies are built through the channels on either side of the TWB, and the currents there will fluctuate with the along-strait pressure gradient applied by the slope anomalies.

2. Data and methods

A total of six pressure gauges—four RBR TGR-2050, one

RBR XR-420-TG (at B2), and one Alec Compact-TD (at B4)—were deployed 30–40 km offshore along the western TWS (Figure 1). The gauges were mounted on the seabed, recording bottom pressure every 10 min. The pressure data were converted directly to heights using a typical sea-water density of 1.026 g cm^{-3} . After truncation for periods of measurement failure, the means were removed from each individual time series. The data were then low-pass filtered with a tidal filter (Thompson, 1983) and subsampled into six-hourly time series (Figure 2).

Because the variation of atmospheric pressure involved in the measurement and the inverse barometer effect are mutually compensated with accuracy (for which 1 hPa corresponds to approximately 1 cm of sea-surface height), no barometer adjustment was applied. This can be justified by comparing the time series of B3 with that of the Xiamen sea level provided by the ECS Branch of State Oceanic Administration and processed in the same manner (Figure 2f).

In addition to the pressure measurement, currents were recorded by a bottom-mounted acoustic Doppler current

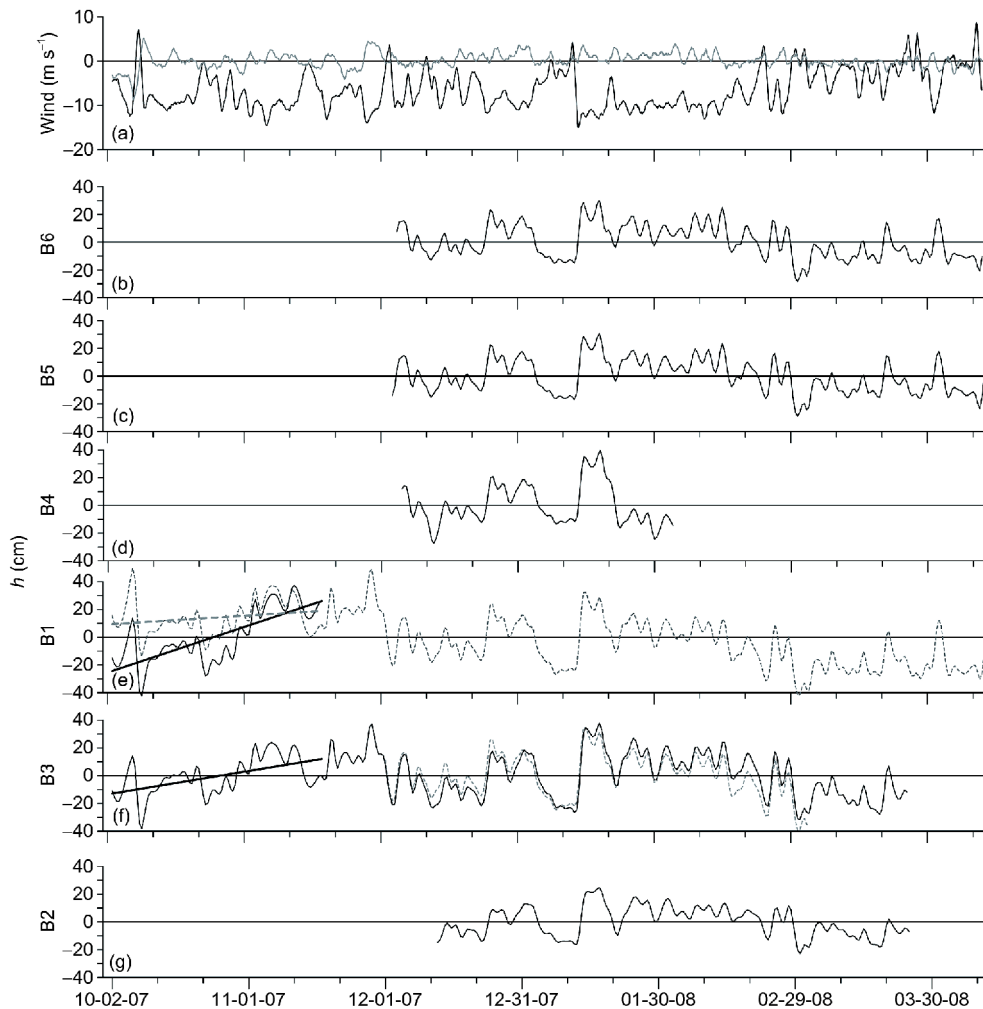


Figure 2 Low-pass filtered time series for (a) north (dark) and east (grey) components of DCD wind, (b) to (g) sea level heights at mooring sites (dark), and (e), (f) Xiamen sea level (grey, in cm). Corresponding time means are removed from each time series.

profiler (ADCP) at B2 as well. The current data were first processed in the same manner as sea levels, and the time series of vertical averaged current in the along-shore direction (50° True) were then computed.

The wind data from the weather stations at Dachendao (henceforth referred to as DCD), an island to the north of the TWS located at 28.45°N , 121.90°E in the ECS (Figure 1), were extracted from the MIDAS Land Surface Stations data of the UK Meteorological Office (available from <http://badc.nerc.ac.uk/data/ukmo-midas>). The original three-hourly data were smoothed with a nine-point moving-average window and resampled at an interval of 6 h. Because the DCD wind is predominately southward with very weak zonal component (Figure 2a), only the meridian (north) wind component was used in the analysis as an indicator of the far-field, large-scale wind field of the winter monsoon.

The interrelationship among various parameters was investigated through time-series analysis by using the classical fast Fourier transform method with a cosine taper (Bendat and Piersol, 1971). Only four out of the six sea-level series (B6, B5, B3, and B2) from early December 2007 to late March 2008 are involved in the analysis because the records from B1 and B4 are too short to give significant results. Segment overlapping was applied to get a higher confidence level when a time series is not long enough to cover four independent segments. The overlapping lengths were limited to less than one sixteenth of the segment length to ensure approximately eight degrees of freedom.

3. Subtidal sea-level variability

The filtered subtidal time series are presented in Figure 2 ordered according to measurement latitude from north to

south. As revealed by previous studies based on coastal tide gauges (Chen and Su, 1987; Li, 1989), the subtidal variations of the time series are remarkably similar and highly correlated all along the TWS. There is also a seasonal fluctuation in sea level in the longer time scale. This is generally positive (above the mean) from mid-January to late February but negative in December and March.

In addition to the correlation in sea levels, it is found that their fluctuations are highly correlated with the north component of the DCD wind (Figure 2). For example, a typical event occurred in the first half of January at all six locations, when sea levels dropped by around 40 cm in about a week and then bounced back sharply by more than 50 cm within two days. That event is obviously correlated with wind variations at DCD, in which the northeastern monsoon began to relax in early January, reversed shortly on January 11, and intensified abruptly right after the reversal. Similar (but less strong) correlated events can also be identified visually from the time series, which generally suggests that sea-level variations roughly 40 km from the mainland coast tend to be correlated but out of phase with the wind forcing. Moreover, their magnitude of fluctuation is comparable with that measured at the coast (Figure 2f).

The above observational results are investigated further by using time-series analysis. The power spectra of the sea-level time series (Figure 3a) are generally “red”. They are energetic in the 2–5-day band, with a major peak at each of 2.9, 3.6, and 4.6 days and a gentler broader band centered at 10.7 days. It is also noted that in the 2–5-day band the energy to the south of the TWB (B2) is much lower than those to the north (B3, B5, and B6). However, in the 10.7-day band, the energy near the TWB (B3) appears to be higher than the others. These differences indicate that the SSL oscillation is more energetic over the northern TWB. Hence, in addition to

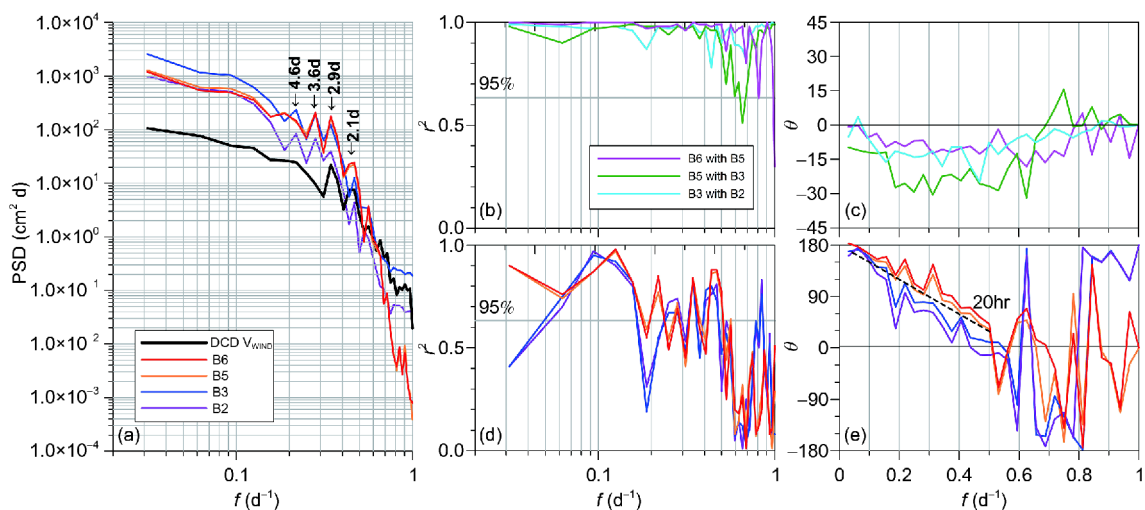


Figure 3 Results of time series analysis: (a) Power spectra of the DCD wind speed (north component) and SSLs at B6, B5, B3 and B2; coherence-squared (b) and phase (c) between sea level pairs of adjacent moorings; and that (d), (e) of the SSLs with the DCD wind speed. Note that curves for B5 and B6 are almost overlapped in panels (a) and (d).

the classical coastal sea-level setup driven by along-shore wind stress (Ekman, 1905; Lentz and Fewings, 2012), the sea-level oscillation may be amplified by geographic features around B3.

The cross-spectral analysis confirms the fact that SSL fluctuations are highly coherent all along the west coast of the TWS (Li, 1989). It further demonstrates that this is true even far from the coast (Figure 3b). The coherence for the given station pairs is generally well above the 95% confidence level and appears especially high at frequencies lower than 0.5 cycles per day (cpd). The phase spectra (Figure 3c) suggest that the SSL signals generally propagate from north to south in that frequency range, whereas at higher frequencies the phase relationship becomes complex and irregular, likely being interfered with by near-inertial oscillation.

The coherence and phase of the pressure time series with that of the meridional wind speed at DCD are also presented in Figure 3. The coherent feature (Figure 3d) can be divided roughly into three frequency sectors: the 0.07–0.5-cpd band (2–14 days) and those above and below it. In the 0.07–0.5-cpd band, the coherence is relatively high, showing a major peak at 10.7 days along with several peaks above the 95% confidence level in the 2–5-day band, suggesting that the large-scale wind field is a major driving force for the 2–14-day fluctuation. Outside that range, the coherence is mostly insignificant except for $f < 0.07$ cpd of B6 with B5 and for the near-inertial band in the southern strait.

The phase spectra (Figure 3e) reveal a linear phase relationship between the pressure series and the DCD wind for $f < 0.5$ cpd. At lower frequencies, the pressure series are 180° out of phase with wind speed, suggesting wind-driven sea-level setup in the western strait. The phase decreases linearly with frequency, suggesting that there is a fixed time lag in sea-level response at each location to winds at DCD. The corresponding time lags estimated based on the 2.1-day coherent band are 17.9, 19.6, 23.5, and 27.3 h for B6, B5, B3, and B2, respectively. The southward-propagating speed of sea-level responses estimated from the increment of time lags between each pair of moorings are 12.8, 16.6, and 8.6 m s⁻¹ between B6 and B5, B5 and B3, and B3 and B2, respectively. Note that the propagation is slower to the south of the TWB.

Because the winter weather systems are coherent structures on a scale much greater than the TWS, which generally propagate southward and eastward at speeds somewhat greater than 10 m s⁻¹ over southeast China (Chen, 1975), the speeds estimated above likely reflect the movement of atmospheric cold fronts and suggest that the observed sea-level fluctuations are basically wind-forced setup and setdown associated with the weather systems. The discrepancies among the speed estimates may be attributed to the changes in shape and moving style of the cold fronts, which tend to

align to the shoreline upon reaching the TWS and slow down toward the south. Moreover, they normally propagate eastward, projecting an up-strait component on the coast that may also result in SSL propagation delays.

In summary, it is evident that there are significant SSL fluctuations in the TWS at roughly 40 km off the coast of the mainland with magnitude comparable to that observed at the coast. The SSL signals are highly coherent all along the strait at periods longer than 2 days and propagate southward in general. For periods of 2–14 days, the SSL is generally coherent with fluctuations of the large-scale wind field, although at a lower level than that between the SSLs themselves. It is thus suggested that the coherent SSL fluctuations in the TWS are mainly forced waves driven by winds associated with the southward-moving weather systems, which prevail over the free coastal trapped waves in the 2–5-day band and dominate the observed sea-level signal (Chen and Su, 1987; Li, 1989).

4. Variability of along-shore sea-level slope

In addition to sea level, the sea-surface slope along the strait should also respond to monsoon fluctuations because of the interaction of wind-driven currents with the topography of the shallow TWB, as discussed in Section 1. Although the absolute slope is not determinable from the measurements made by our mooring array, the deviation (i.e., the slope anomaly) from its mean status can be derived. That provides a unique opportunity to examine the response of the along-shore sea-level slope under the combined forcing of winter monsoon and topography, which to our knowledge has never been investigated before. In the following discussion, the subtidal variation of the along-shore slope anomaly is represented by the sea-level difference (Δh) of the mooring pair under consideration, among which significant difference was found between the two sides of the TWB.

4.1 Slope variation to the north of the TWB

To the north of the TWB, the variation of slope anomaly is given by the sea-level differences of B6 from B5 (Δh_{B6-B5}) and B5 from B3 (Δh_{B5-B3}), which show that the slopes vary synchronously and in phase with that of the north component of the DCD winds (Figures 4a, b and 5a, b). Note that although the magnitude of fluctuation Δh_{B5-B3} is about three times that of Δh_{B6-B5} , the discrepancy in slope is not that large because the distance between B5 and B3 is greater (Figure 1). The slope magnitudes estimated from the sea-level differences are of the order of 10⁻⁷ and (mutually) positively correlated (Figure 6a). A regression through the origin gives a ratio of 0.48, indicating that the slope-fluctuation magnitude closer to the TWB is about twice that further north.

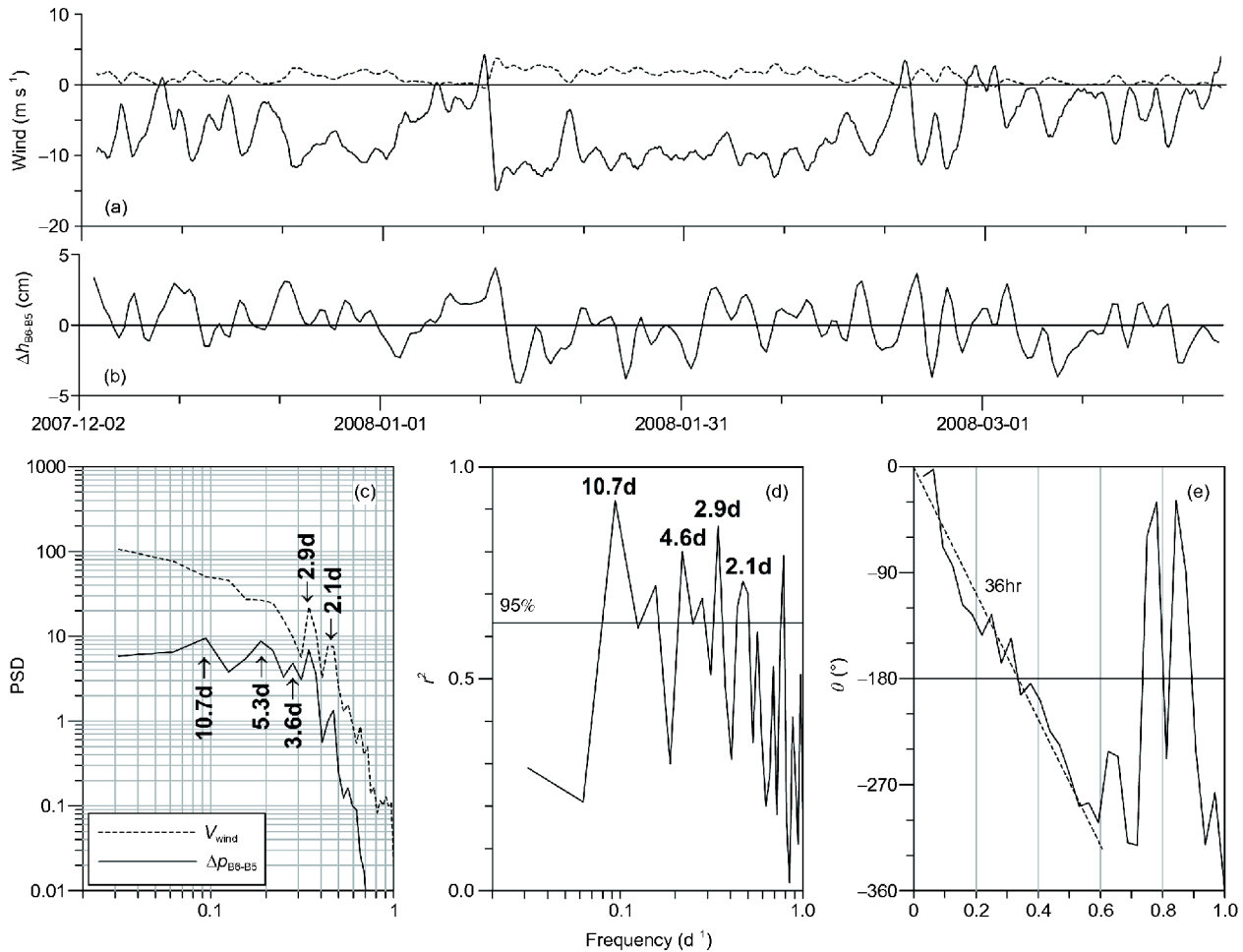


Figure 4 Low-pass filtered time series of the (a) north (solid line) and east (dash line) wind speed components at DCD and (b) the SSL difference of B6 from B5. The results of the cross-spectral analysis of the north wind component and Δh_{B6-B5} : (c) Power spectra, (d) coherence-squared, and (e) phase. Frequency interval: $1/32 \text{ d}^{-1}$; degrees of freedom: 8.

Analyses in the frequency domain show that the power spectra of both time series are energetic in the 2–5-day band (with peaks at 2.1, 2.9, 3.6, and 5.3 days) and the 10.7-day band (Figures 4c and 5c) but their shapes are rather different. The spectrum of Δh_{B6-B5} looks rather flat at periods longer than 5 days (Figure 4c) but appears quite red for Δh_{B5-B3} (Figure 5c). The difference also suggests stronger fluctuation of along-shore slope close to the TWB, especially at lower frequencies.

The cross-spectral analyses show that the slope fluctuation is generally coherent at the 95% significant level with the DCD wind speed at all energetic bands indicated above (Figures 4d and 5d), and that, for frequencies lower than 0.5 cpd, the phase lag increases linearly with frequency (Figures 4e and 5e). The linear phase–frequency relationship implies that slope variation to the north of the TWB generally lags the wind by 36 h. This means that a southward slope anomaly to the north of the TWB is fully built 36 h after a northerly wind event, when water is piled up over the TWB by the wind-driven transport.

4.2 Slope to the south of the TWB

The variation of along-shore sea-level slope to the south of the TWB is given by the sea-level differences of B3 from B2 (Δh_{B3-B2} ; Figure 7b). Similar to Δh_{B5-B3} , its power spectrum appears red (Figure 7c) and shows a group of energetic peaks in the 2–5-day band located at 4.6, 3.6, 2.9, and 2.1 days and a gentler peak at 10.7 days. Moreover, the subtidal fluctuation is also coherent with the DCD wind. Significant coherence was found in a broad band ranging from 6.4 to 16.0 days and the three minor peaks at 2–3 days (Figure 7d).

The most remarkable feature of the time series of Δh_{B3-B2} is that, unlike those to the north of the TWB, it varies synchronously but out of phase with the DCD wind speed (Figure 7a and b). This is further verified by the cross-spectral analysis, which shows a linear phase–frequency relationship for periods longer than 2 days that crosses the vertical axis at 180° (Figure 7e). This means that, just opposite to the two series to the north, a northerly wind event will result in a northward slope anomaly to the south of the

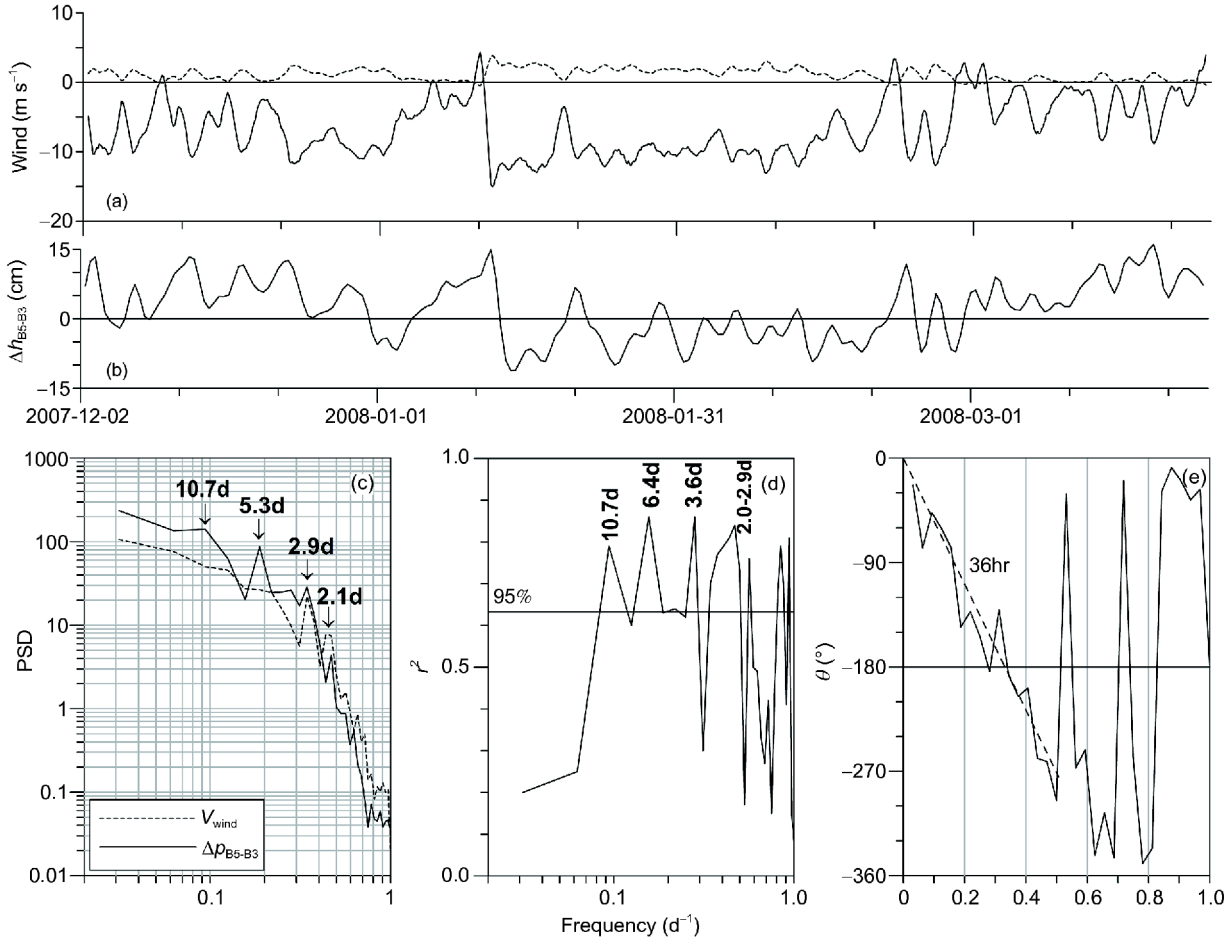


Figure 5 Low-pass filtered time series of the (a) north (solid line) and east (dash line) wind speed components at DCD and (b) the SSL difference of B5 from B3. The results of the cross-spectral analysis of the north wind component and Δh_{B5-B3} : (c) Power spectra, (d) coherence-squared, and (e) phase. Frequency interval: $1/32 \text{ d}^{-1}$; degrees of freedom: 8.

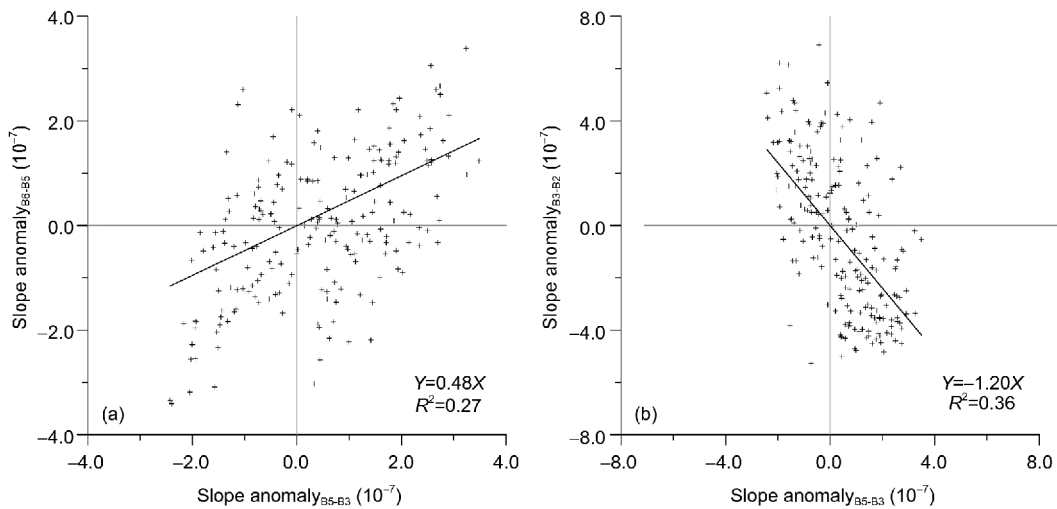


Figure 6 Correlations of sea level slope anomalies of B6 from B5 (a) and B3 from B2 (b) with that of B5 from B3 showing that slope variation on the two sides of the TWB is in the opposite direction.

TWB. Furthermore, the linear relationship gives a time lag of 20 h, implying a much-shorter response time than that to the north of the TWB.

The phase difference is further demonstrated in Figure 6b, which shows that the slopes on the two sides of the TWB are negatively correlated. It is thus evident that the subtidal re-

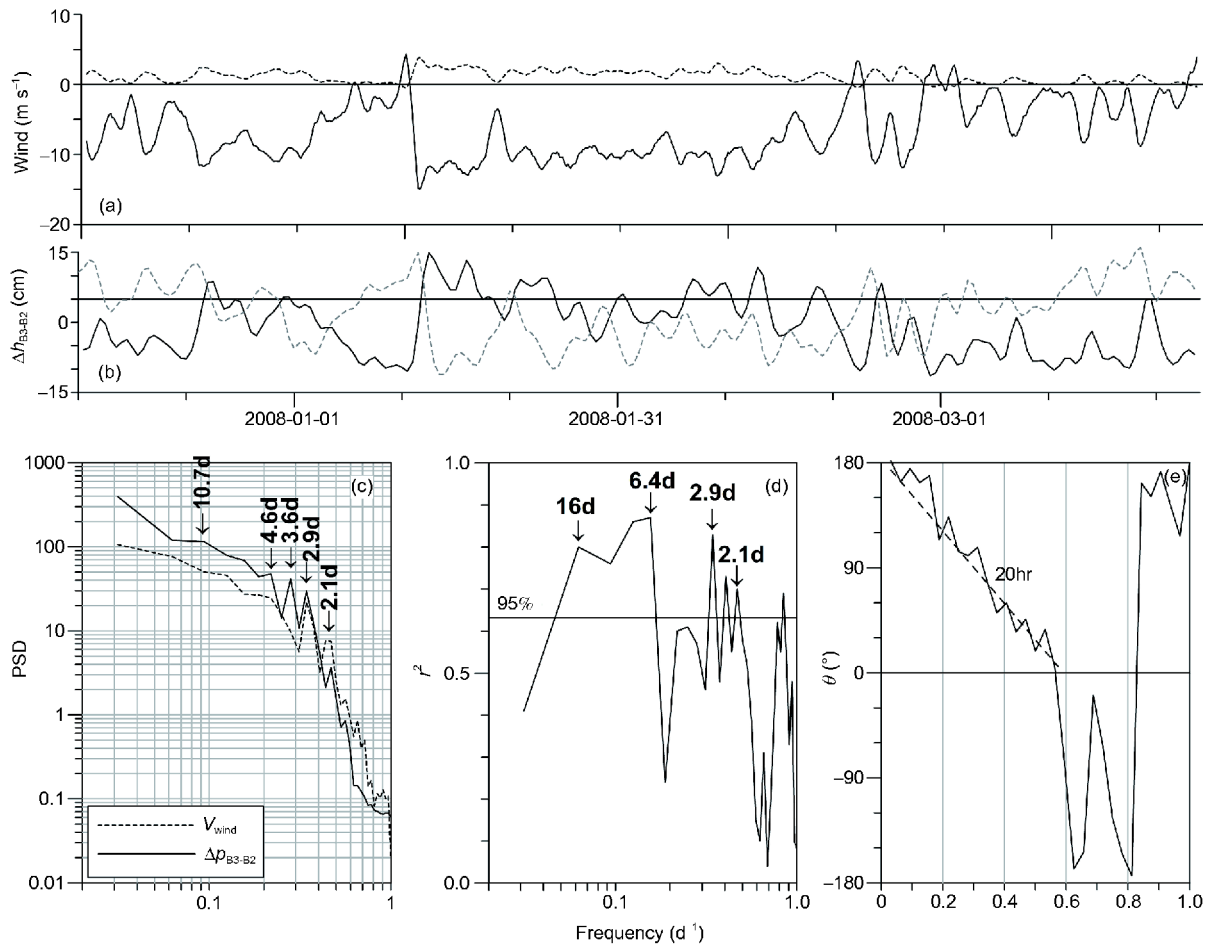


Figure 7 Low-pass filtered time series of the (a) north (solid line) and east (dash line) wind speed components at DCD and (b) the SSL difference of B3 from B2. The results of the cross-spectral analysis of the north wind component and Δh_{B3-B2} : (c) Power spectra, (d) coherence-squared, and (e) phase. Frequency interval: $1/32 \text{ d}^{-1}$; degrees of freedom: 8.

sponses of the along-shore sea-level slope anomaly to winter monsoon fluctuations are in opposite directions on the two sides of the TWB and that their response mechanisms may differ. In addition, it is suggested that the TWB plays a key role in controlling the sea-level fluctuations in the TWS and the subtidal currents that are induced.

4.3 Effect of topography

Topography is an important factor that affects circulation in the coastal ocean. A great deal of work in the past has addressed subtidal flows along relatively straight coasts with smooth topography. However, for complex topography our understanding is rather limited (Trowbridge et al., 1998). A strait is an important type of topography, often marking a natural boundary in an ocean system. Because of restrictions in width or depth, the interaction of a strait flow with topography results in a range of important flow phenomena (Lane-Serff, 2004).

For the TWS, the winter water column is vertically

homogeneous in general, and the strait flows fluctuate with the strength of the northeast monsoon (Lin et al., 2005; Pan et al., 2013). The wind-forced surge waves will propagate southward along the strait following the weather system. On approaching the TWB, the surge waves will interact with the topography and pile water up on the northern slope of the TWB.

Hence, in addition to the wind-driven cross-shore sea-level setup and setdown at the western coast of the TWS, there are also along-strait sea-level setup and setdown caused by interaction of wind-driven currents with the topography. Because of blocking by the TWB, the southward current generated during a northerly wind event will produce a southward along-shore slope anomaly to the north of the TWB, where the water level is the highest (Liao et al., 2013). On the other side of the bank, a slope anomaly is also built but in the opposite (northward) direction. As the wind relaxes, the southward current decreases and may even reverse. The sea level falls over the TWB, and so do the slope-anomaly amplitudes on either side of the TWB.

It is interesting to note that the response time of sea-level slope to wind forcing on the upstream/northern side of the TWB (36 h; **Figures 4e and 5e**) is different from its downstream/southern side (20 h; **Figure 7e**). Because the response time of sea levels to the north of the TWB to the DCD wind is around 20 h (23.5 h for B3; see Section 3 and **Figure 3c**), it is likely that the response of the sea-level slope to the south of the TWB is mainly a passive result of the oscillating sea level over the TWB. Moreover, a northeasterly wind event will drive water away from the bank that may further speed up the downstream slope variation in the southern TWB and reduce the response time. By contrast, a longer time is needed for the slope to be built to the north of the TWB. This is because the sea level may still remain high in the northern strait while the surge from the north is piling water over the TWB and the slope is yet to be built.

5. Flow in the channels on either side of the TWB

Because of the along-shore sea-level setup and setdown over the TWB, a change of along-channel pressure gradient is applied to the channels on either side of the TWB (the WCh and PHCh), which is expected to cause the current through the channels to fluctuate.

In the WCh, a well-established linear relationship was observed between the vertically averaged along-channel current component at B2 and the anomalous pressure difference of B3 from B2 (**Figure 8a**). A linear fit gives $v_{B2} = -2.44 \times \Delta h_{B3-B2} - 4.92$ with the coefficient of determination $R^2 = 0.82$. As indicated by **Oey et al. (2014)**, the along-channel current is driven by both along-channel pressure gradient and along-shore wind stress, while the cross-chan-

nel current is negligible in the TWS in winter. It is thus evident that during winter the subtidal current through the channel to the west of the TWB is influenced significantly by the along-channel pressure-gradient anomaly resulting from interaction of monsoon-driven currents with the shallow TWB. It is also shown by the y-intercept that the depth-integrated mean current is about 5 cm s^{-1} southward during the analyzed period from early December 2007 to late March 2008. It is likely that, in addition to fluctuation on the subtidal scale, the seasonal mean flow through the WCh may also be induced by the sea-level gradient along the channel built after the onset of the winter monsoon. In fact, a rising trend in sea level is clearly visible in B1 and B3 from early October to November (**Figure 2e and f**), suggesting possible seasonal pile-up to the north of the TWB that drives the southward mean flow through the WCh. This trend also appears at the Xiamen coastal station but with a lower rate (**Figure 2e**, dashed line), which implies that the pile-up process is more intense offshore, being induced by the TWB.

A linear regression of the along-channel flow with the DCD wind (**Figure 8b**) shows a weak coefficient of determination ($R^2 = 0.4$), which is much less than that with the slope anomaly. It is thus suggested that even though wind is the main driving force of the coastal current of the TWS, the variability of along-channel pressure gradient appears to be a more important driving force of the flow variability along the WCh, while the coastal current interacts with the TWB.

Similarly, the sea-level variation built by the along-shore wind setup will exert a change of along-shore pressure gradient on the PHCh and may cause current fluctuations on both subtidal and seasonal time scales. Previous observations in the PHCh have shown strong short-period current fluctuations on top of the Kuroshio-driven mean flows, which

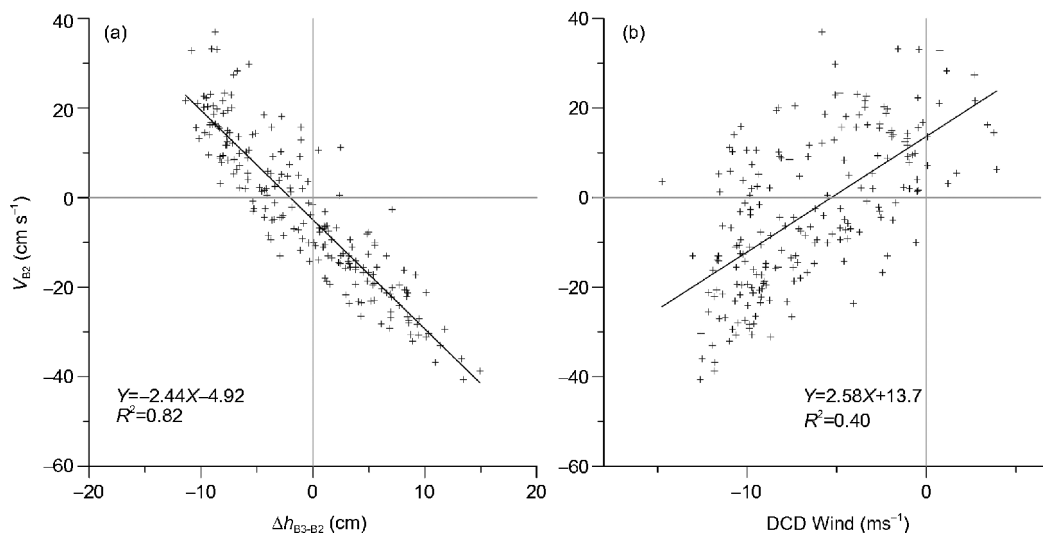


Figure 8 Correlation of the vertical mean current along the channel to the west of the TWB measured at mooring B2 with the sea level difference of B3 from B2 (a), and the DCD wind (b).

are well correlated with wind-stress variations caused by the passage of cold fronts (Chuang, 1985, 1986). However, the situation must be more complicated because of the competition between the monsoon-induced pressure gradient and the opposite gradient induced by Kuroshio intrusions to the south of the PHCh on different time scales (Li and Wu, 1989; Li et al., 1998; Shaw, 1989).

6. Discussion and conclusions

Based on observations from a series of pressure gauges deployed along a line about 40 km off the mainland coast, the features of winter subtidal variability in the TWS were investigated. We draw the following conclusions from the results. (1) In the TWS, there are significant SSL fluctuations at roughly 40 km off the mainland with magnitude comparable to that at the coast. They are highly coherent all along the strait and are mainly forced waves driven by winds associated with fluctuations of the monsoon system. (2) In addition to the normal lateral wind setup, there is also significant along-shore sea-level setup caused by combined forcing of winter monsoon and topography of the TWB. (3) Because of blocking by the TWB, a northerly wind event will drive a southward current surge and produce a southward sea-level slope anomaly in the northern TWB, whereas a slope anomaly is also built in the southern bank but in the opposite (northward) direction. This process weakens and may even reverse as the wind relaxes. (4) Subtidal current through the channel to the west of the TWB is closely related to the along-channel pressure gradient through the channel, and the seasonal mean current may be the same. (5) As the most important topographic feature in the TWS, the TWB has a strong impact on the circulation of the TWS and the water exchange between the China Seas.

A problem left unexplained concerns the 32-day band (Figure 3d, covering 21.3-day to 64-day oscillations). It is noted that, in this band, the coherence of sea level with wind (Figure 3c, covering 21.3-day to 64-day oscillations) is significant at B5 and B6 but insignificant at B3 and B2. As for the sea-level slope, it is not coherent with wind at all in the 32-day band. This suggests that, at the lower end of the observed frequency band, fluctuations in the southern strait may be caused by a different mechanism from that of the northern strait. Previous studies have reported energetic sea-level fluctuations in the equivalent bands along the coasts of southern Taiwan and the northern South China Sea (Li, 1993; Shih et al., 1986) and have discovered that this signal appears earlier in the south strait (Li, 1989). Hence, the 32-day fluctuation may originate from the area to the south of the TWB that is not driven by the wind. Instead of the wind stress, the observed discrepancy may be caused by certain physical processes of the SCS, such as the Kuroshio intru-

sion (Farris and Wimbush, 1996; Li and Wu, 1989) and eddy shedding (Jia and Liu, 2004; Li et al., 1998).

A further question is what happens to the north of the TWB while the northerly wind is weakening and the surge is retreating. Some of our observations suggest that the retreating current may turn offshore and the signal may propagate eastward, leading to significant cross-shore transport of low-temperature coastal water to the east and resulting in cold disaster for the tropical ecosystem around Penghu (Chang et al., 2009; Hsieh et al., 2008; Liao et al., 2013). Further investigation is underway to address these issues.

Acknowledgements This work was supported by National Natural Science Foundation of China (Grant Nos. 41476005 & U1305231). The field work was supported by Chinese Offshore Physical Oceanography and Marine Meteorology Investigation and Assessment Project (Grant No. 908-ZC-I-01).

References

- Bendat J S, Piersol A G. 1971. Random Data: Analysis and Measurement Procedures. New York: John Wiley & Sons
- Chang Y, Lee K T, Lee M A, Lan K W. 2009. Satellite observation on the exceptional intrusion of cold water in the Taiwan Strait. *Terr Atmos Ocean Sci*, 20: 661–669
- Chen C K. 1975. A study of the movement of cold fronts and associated precipitation along the coast southeast China. *Atmosph Sci*, 2: 9–21
- Chen D K, Su J L. 1987. Continental shelf waves study along China coast (in Chinese). *Acta Oceanol Sin*, 9: 1–15
- Chuang W S. 1985. Dynamics of subtidal flow in the Taiwan Strait. *J Oceanogr*, 41: 65–72
- Chuang W S. 1986. A note on the driving mechanisms of current in the Taiwan Strait. *J Oceanogr*, 42: 355–361
- Ekman V W. 1905. On the influence of the earth's rotation on ocean currents. *Ark Mat Astron Fys*, 2: 1–53
- Farris A, Wimbush M. 1996. Wind-induced Kuroshio intrusion into the South China Sea. *J Oceanogr*, 52: 771–784
- Garrett C, Toulany B. 1982. Sea level variability due to meteorological forcing in the northeast Gulf of St. Lawrence. *J Geophys Res*, 87: 1968–1978
- He Y, Cai S, Wang D, He J. 2015. A model study of Luzon cold eddies in the northern South China Sea. *Deep-Sea Res Part I-Oceanogr Res Pap*, 97: 107–123
- Hong B, Wang D. 2006. Diagnostic analysis on the northern South China Sea winter counter-wind current. *Chin Sci Bull*, 51: 9–16
- Hsieh H J, Hsien Y L, Jeng M S, Tsai W S, Su W C, Chen C A. 2008. Tropical fishes killed by the cold. *Coral Reefs*, 27: 599–599
- Hu J, Kawamura H, Li C, Hong H, Jiang Y. 2010. Review on current and seawater volume transport through the Taiwan Strait. *J Oceanogr*, 66: 591–610
- Jacobs G A, Preller R H, Riedlinger S K, Teague W J. 1998. Coastal wave generation in the Bohai Bay and propagation along the Chinese coast. *Geophys Res Lett*, 25: 777–780
- Jan S, Wang J, Chern C S, Chao S Y. 2002. Seasonal variation of the circulation in the Taiwan Strait. *J Mar Syst*, 35: 249–268
- Jia Y, Liu Q. 2004. Eddy shedding from the Kuroshio Bend at Luzon Strait. *J Oceanogr*, 60: 1063–1069
- Ko D S, Preller R H, Jacobs G A, Tang T Y, Lin S F. 2003. Transport reversals at Taiwan Strait during October and November 1999. *J Geophys Res*, 108: 3370
- Lane-Serff G F. 2004. Topographic and boundary effects on steady and unsteady flow through straits. *Deep-Sea Res Part II-Top Stud Oceanogr*, 51: 321–334

- Lentz S J, Fewings M R. 2012. The wind- and wave-driven inner-shelf circulation. *Annu Rev Mar Sci*, 4: 317–343
- Li L. 1989. A study of winter subtidal sea level fluctuation in the Taiwan Strait. *Acta Oceanol Sin*, 11: 275–283
- Li L, Wu B Y. 1989. A Kuroshio loop in South China Sea?—On circulations of the north-eastern South China Sea (in Chinese with English abstract). *J Oceanogr in Taiwan Strait*, 8: 89–95
- Li L. 1993. A study on winter subtidal sea level fluctuation along the northern coast of the South China Sea (in Chinese with English abstract). *Tropic Oceanogr*, 12: 52–60
- Li L, Nowlin Jr. W D, Jilan S. 1998. Anticyclonic rings from the Kuroshio in the South China Sea. *Deep-Sea Res Part I-Oceanogr Res Pap*, 45: 1469–1482
- Liao E H, Jiang Y W, Li L, Hong H S, Yan X H. 2013. The cause of the 2008 cold disaster in the Taiwan Strait. *Ocean Model*, 62: 1–10
- Lin S F, Tang T Y, Jan S, Chen C J. 2005. Taiwan strait current in winter. *Cont Shelf Res*, 25: 1023–1042
- Oey L Y, Chang Y L, Lin Y C, Chang M C, Varlamov S, Miyazawa Y. 2014. Cross flows in the Taiwan Strait in Winter. *J Phys Oceanogr*, 44: 801–817
- Pan A J, Wan X F, Guo X G, Jing C S. 2013. Responses of the Zhe-Min coastal current adjacent to Pingtan Island to the wintertime monsoon relaxation in 2006 and its mechanism. *Sci China Earth Sci*, 56: 386–396
- Pratt L J, Helfrich K R, Chassignet E P. 2000. Hydraulic adjustment to an obstacle in a rotating channel. *J Fluid Mech*, 404: 117–149
- Qiu C, Wang D, He Z, Chen C. 2012. Seasonal variability of chlorophylla fronts in the Luzon Strait based on satellite observations. *Aquatic Ecosyst Health Manage*, 15: 46–52
- Shao H, Li Y, Li L. 2011. Sun glitter imaging of submarine sand waves on the Taiwan Banks: Determination of the relaxation rate of short waves. *J Geophys Res*, 116: C06024
- Shaw P T. 1989. The intrusion of water masses into the sea southwest of Taiwan. *J Geophys Res*, 94: 18213–18226
- Shi R, Guo X, Wang D, Zeng L L, Chen J. 2015. Seasonal variability in coastal fronts and its influence on sea surface wind in the Northern South China Sea. *Deep-Sea Res Part II-Top Stud Oceanogr*, 119: 30–39
- Shih C F, Shaw P T, Li H W. 1986. Low Frequency sea level fluctuations around Taiwan (in Chinese). *Acta Oceanogr Taiwanica*, 17: 18–28
- Thompson R O R Y. 1983. Low-pass filters to suppress inertial and tidal frequencies. *J Phys Oceanogr*, 13: 1077–1083
- Trowbridge J H, Chapman D C, Candela J. 1998. Topographic effects, straits and the bottom boundary layer. In: Brink K H, Robinson A R, eds. *The Sea*. New York: John Wiley and Sons. 63–88
- Wang D, Liu Y, Qi Y, Shi P. 2001. Seasonal variability of thermal fronts in the northern South China Sea from satellite data. *Geophys Res Lett*, 28: 3963–3966
- Wang D, Xu H, Lin J, Hu J. 2008. Anticyclonic eddies in the northeastern South China Sea during winter 2003/2004. *J Oceanogr*, 64: 925–935
- Wang D, Hong B, Gan J, Xu H. 2010. Numerical investigation on propulsion of the counter-wind current in the northern South China Sea in winter. *Deep-Sea Res Part I-Oceanogr Res Pap*, 57: 1206–1221
- Wang D, Shu Y, Xue H, Hu J, Chen J, Zhuang W, Zu T T, Xu J. 2014. Relative contributions of local wind and topography to the coastal upwelling intensity in the northern South China Sea. *J Geophys Res-Oceans*, 119: 2550–2567
- Wang J, Chern C S. 1988. On the Kuroshio branch in the Taiwan strait during wintertime. *Prog Oceanogr*, 21: 469–491
- Wang J, Chen C S. 1989. On cold water intrusions in the eastern Taiwan Strait during the cold season (in Chinese with English abstract). *Acta Oceanogr Taiwanica*, 22: 43–67
- Wang Y H, Chiao L Y, Lwiza K M M, Wang D P. 2004. Analysis of flow at the gate of Taiwan Strait. *J Geophys Res*, 109: C02025
- Zhao B R, Cao D M. 1987. Wintertime low frequency fluctuations of Chinese coastal sea-level in the Huanghai sea and the East China Sea. *Oceanol Limnol Sin*, 18: 563–574

(Responsibility editor: Dongxiao WANG)